Simultaneous Acquisition of Emission and Transmission Data for Improved Thallium-201 Cardiac SPECT Imaging Using a Technetium-99m Transmission Source

Eric C. Frey, Benjamin M.W. Tsui and J. Randolph Perry

Department of Biomedical Engineering and Department of Radiology, The University of North Carolina at Chapel Hill, North Carolina

Transmission computed tomography (TCT) data provides useful complementary information to single-photon emission computed tomography (SPECT) reconstructions, especially for cardiac studies. In particular, TCT data has been used to correct for nonuniform attenuation in the chest. Typically the transmission data are acquired in a separate acquisition, but simultaneous acquisition is preferable both to save time and to avoid difficulties involved with registration. In this work, we present a technique for simultaneously acquiring ^{201}Tl SPECT and TCT data using a ^{99m}Tc sheet source that requires only minor equipment modifications. The use of these isotopes results in cross-contamination of the emission and transmission data. We present a practical technique to compensate for this contamination using postacquisition image processing. This technique was evaluated by performing phantom and patient studies. The resulting images compare well with data obtained from separate emission and transmission studies.

J Nucl Med 1992; 33:2238–2245

P hoton attenuation is the most important factor degrading the quantitative accuracy of SPECT images. It also results in a degradation of image quality through the introduction of image artifacts and distortions. In cardiac SPECT the effects of photon attenuation are especially complex due to the nonuniform attenuation distribution in the thorax. Conventional attenuation compensation techniques assume a uniform attenuation distribution and thus do not apply. Accurate attenuation compensation in cardiac SPECT requires measurement of the attenuation distribution and the use of iterative reconstruction techniques (1–3).

One method of estimating the attenuation distribution in the patient is transmission computed tomography (TCT). Typically, transmission data is acquired in a separate study using either a gamma camera and flood source (2), or conventional x-ray CT equipment (4). However, this extra acquisition is undesirable in a clinical setting and may result in misregistration of the two data sets due to patient movement between the studies.

Two methods for simultaneously acquiring the emission and transmission data in ^{99m}Tc SPECT have been proposed: the use of dual isotopes (5) and a scanning line source (6). In the dual-isotope technique, a transmission source isotope is used that emits a lower energy photon than the emission source, but for ^{201}Tl SPECT, there are no suitable isotopes emitting gammas with energies lower than the 75 keV ^{201}Tl photons. In the scanned line source technique, a high intensity ^{99m}Tc line source is scanned across the field of view during the emission acquisition. A strip of the detector area directly opposite the line source is acquired into the transmission image; the remainder of the detector area is collected into the emission image. The synchronized movement of the line source and the acquisition strip eliminates contamination of the emission data, but this technique requires significant equipment modifications.

In this paper, we present a technique for simultaneously acquiring ^{201}Tl emission and transmission data using a ^{99m}Tc transmission source. The advantages of this technique are that ^{99m}Tc is inexpensive, readily available, has good imaging properties and, most importantly, no major equipment modifications are necessary. However, this combination of isotopes does result in cross-contamination between the emission and transmission projection data and data processing techniques have been developed to compensate for this cross-talk. These techniques were applied to experimental phantom and patient data in order to demonstrate their effectiveness.

MATERIALS AND METHODS

Cross-Contamination of Transmission and Emission Data

When ^{201}Tl decays, it emits 68-83 keV Hg x-rays as well as 135 and 167 keV gamma rays. The photons in the low energy peak comprise approximately 88% of the emitted photons and provide the majority of the emission data. Since the 140 keV photon from the ^{99m}Tc has a higher energy than the Hg x-rays and overlaps the ^{201}Tl gamma peaks, there will be some cross-contamination of the emission and transmission data, as mentioned above.

One mechanism for contamination of the emission data by ^{99m}Tc photons is scatter inside the patient. Since the backscattering edge for a 140 keV photon is 90 keV, only ^{99m}Tc photons scattered through angles close to 180° have energies low enough to be detected in the 64-86 keV window. As a result of the source collimation, singly scattered ^{99m}Tc reaching the camera will have undergone scattering with angles less than 90°. Thus only multiply scattered transmission source photons will contribute to the emission data.

The emission data are also contaminated as a result of interactions with the source and camera collimators. Both scattered and unscattered ^{99m}Tc photons interact with the collimators, resulting in the production of Pb x-rays with energies in the range 72-88 keV. These x-rays will be detected in the emission energy window and cause contamination of the ^{201}Tl emission data.

Contamination of the transmission data is from the 135 and 167 keV ^{201}Tl photons. Due to finite energy resolution of the detector, a fraction of both unscattered 135 keV photons and scattered 135 and 167 keV photons are detected in the transmission energy window.

Method for Cross-Contamination Compensation

A technique for compensating for the cross-contamination has been developed. The total number of photons detected in the 64-86 keV emission energy window, Em, is the sum of: (1) the true emission data, E; (2) multiply scattered ^{99m}Tc photons; and (3) Pb x-ray photons excited by the ^{99m}Tc photons. As a first approximation, we assume that the contamination caused by (2) and (3) is proportional to T, the true transmission data, thus:

$$E_m = E + f_E T, \qquad \text{Eq. 1}$$

where f_E is the emission correction factor.

Similarly, the total counts measured in the transmission energy window, T_m, is equal to the sum of counts from: (1) the true transmission data, T; (2) scattered 135 and 167 keV ^{201}Tl photons; and (3) unscattered 135 and 167 keV ^{201}Tl photons. We assume that the contamination of the emission window is proportional to the true emission data, E:

$$T_m = T + f_T E, \qquad \text{Eq. 2}$$

where f_T is the transmission correction factor.

With these approximations, it is possible to derive an expression for the cross-contamination compensated emission and transmission data, E_c and T_c, respectively:

$$E_c = \frac{E_m - f_E T_m}{1 - f_E f_T}, \qquad \text{Eq. 3}$$

and

$$T_c = \frac{T_m - f_T E_m}{1 - f_E f_T}. \qquad \text{Eq. 4}$$

By using Equations 3 and 4, we can compensate for the cross-contamination if we know the emission and transmission corrections factors, f_E and f_T, respectively. The determination of these factors and the validity of the approximations in Equations 1 and 2 are discussed below.

Data Acquisition

To determine the correction factors and evaluate the technique, both phantom and patient studies were performed. Data were acquired using a GE 400 AC/T SPECT system (General Electric Medical Systems, Milwaukee, WI). The transmission data were acquired using a flood phantom (sheet source) filled with a solution containing ^{99m}Tc. The flood source was attached to the gantry on the opposite side of the patient and fitted with a collimator (3). This source collimator reduces the number of scattered ^{99m}Tc photons and the patient dose.

With this SPECT system, only two images can be acquired simultaneously and each image can come from one energy window. As a result, the 167 keV Tl photons were ignored and the emission and transmission data were acquired from 75 ± 11 keV and 140 ± 14 keV energy windows, respectively.

Projection data were acquired into a 64 × 64 matrix with 0.62 cm pixels and were uniformity corrected during data acquisition. For SPECT studies, the data were acquired at 64 views over 180° from 45° left posterior oblique (LPO) to 45° right anterior oblique (RAO). The collimator used was specially designed for Tl studies (7) with a 20% higher sensitivity and a 10% lower spatial resolution than a GE low-energy, general-purpose (LEGP) collimator.

Phantom Studies

Three phantoms were used to evaluate the simultaneous acquisition technique. A chest phantom, composed of a cylindrical phantom with elliptical cross section, a cardiac insert (Data Spectrum Model 2230, Data Spectrum Corp., Chapel Hill, NC) and lung inserts (3), was used to simulate the activity and attenuation distribution in a patient. A uniform water-filled cylindrical phantom with a circular cross section (Data Spectrum SPECT Phantom with inserts removed) and a sheet phantom consisting of four to forty 6-mm thick Lucite sheets were used to evaluate the dependence of the emission correction factor on phantom size and shape.

For the chest phantom both simultaneously and separately acquired transmission and emission data were collected. In all cases, projection data were acquired with an acquisition time of 40 sec per view using the data acquisition parameters described in the previous section. The chest phantom was filled with water (no activity), the transmission source filled with 30 mCi of ^{99m}Tc, and transmission data were acquired. Next, the body of the phantom and the outer chamber of the cardiac insert were filled with a total of 1 mCi of ^{201}Tl. The ratio of the activity concentration in the body of the phantom to that in the outer chamber of the cardiac insert was 1 : 6.8 to simulate ^{201}Tl uptake. A set of simultaneously acquired emission-transmission data was collected. The transmission source was then removed and a separate set of emission data were acquired using the hot phantom. Finally, a 15-min static image of the flood source was acquired for use in transmission data preprocessing.

For the uniform circular phantom, a transmission study was acquired for 40 sec per view using the cold phantom (no activity) and the flood source filled with 20 mCi of ^{99m}Tc.

For the sheet phantom, static transmission images were acquired using the flood source filled with 30 mCi of ^{99m}Tc and an acquisition time of 120 sec.

Patient Study

A protocol similar to that used for the chest phantom was also used to collect patient data. The patient was injected with 2.0 mCi of ^{201}Tl. Approximately three hours later, simultaneous emission and transmission projection data were acquired using the ^{99m}Tc transmission source filled with an activity of 20 mCi and the energy windows and acquisition parameters described previously. Data were acquired for 23 sec per view. During data acquisition, the patient was allowed to keep her arms at her side in order to reduce the discomfort resulting from the additional study. Next, the transmission source was removed and separate emission data were acquired, again for 23 sec per view. Since the emission-only data were used diagnostically, the patient was asked to keep her hands over her head in order to avoid the loss of image quality caused by attenuation in the arms. In the emission-only study, the 135 and 167 keV Tl photons were added to low energy photons to form the emission image, resulting in a significant increase ($\approx$25%) in the count rate. Due to these two differences, the separately acquired emission data is less noisy than the emission data from the simultaneous study. Finally, a 15-min static image of the flood source was acquired after the patient data acquisition.

Correction Factor Determination

The emission and transmission correction factors, f_E and f_T, were determined using data obtained in separate emission or transmission only studies. For example, with the transmission source only present, the photons counted in the emission window are due solely to the contamination by the transmission source.

From the emission source only experiment, the emission correction factor was estimated as the ratio of the counts in the emission window divided by counts in the transmission window. This method gives smaller error values in the correction factor than does the fitting method used for the transmission correction factor.

The transmission correction factor was studied in experiments using only the emission source. The transmission correction factor was determined by plotting the counts in the transmission window on the y-axis versus the counts in emission window for each pixel. The correction factor was determined from this plot by fitting a line with y-intercept equal to zero using a weighted least squares technique. The weighted fitting technique was used because there was a small number of counts in the transmission window.

Image Reconstruction and Processing

In addition to the cross-contamination of the emission and transmission data, other problems arising in reconstructing both separately and simultaneously acquired emission and transmission data are noise amplification caused by the subtraction based compensation scheme, truncation of the patient projection data, and the effects of nonuniform attenuation. In this work these problems were addressed by the use of the following image processing techniques and reconstruction algorithms.

The subtraction step used in the compensation scheme causes an increase in image noise. As a result, the compensation scheme can give rise to zero or negative pixel values. For the emission data, negative values were truncated to zero prior to reconstruction.

It is especially important to handle the zero and negative pixels properly for the transmission projection data, because transmission data are preprocessed by dividing the counts in each pixel by the corresponding incident intensity and taking the natural logarithm. To avoid zero or negative pixels, we noted that the number of transmitted photons is small, corresponding to a large value of line integral of the attenuation coefficient through the object. For this reason, pixels in the preprocessed transmission projection data corresponding to values less than or equal to zero in the raw data were replaced by the average of the 30 largest pixel values in the preprocessed image from the same projection view.

Both the filtered backprojection (FB) and the iterative maximum-likelihood expectation-maximization (ML-EM) (8,9) reconstruction algorithms were used. The FB algorithm was used to reconstruct the phantom transmission data and emission data without attenuation compensation. For the patient, the 40 cm diameter circular field of view resulted in truncated projections. To better handle the truncated data, the ML-EM algorithm was used for both emission and transmission reconstructions. Reduction in truncation artifacts was accomplished with ML-EM by not setting projection data outside the sensitive area of the camera to zero.

Nonuniform attenuation compensation for both phantom and patient data was accomplished using ML-EM algorithm combined with a projector-backprojector that modeled nonuniform attenuation (1). Since the transmission data were acquired with 140 keV photons and the emission data with 75 keV photons, the measured attenuation map was scaled by the ratio of the attenuation coefficient of water at 75 keV divided by that at 140 keV. In addition, any negative values in the attenuation map data, resulting from either the use of the FB reconstruction algorithm or post-reconstruction filtering, were truncated to zero.

A three-dimensional Butterworth filter was applied to the reconstructed images to reduce image noise. An order of 8 and a cutoff frequency of 0.24 pixel^{-1} for the phantom data and 0.22 pixel^{-1} for the patient data were used.

RESULTS AND DISCUSSION

Emission Correction Factor

The emission correction factor, f_E, was determined from the transmission source only experiments. Data from the chest, circular, and sheet phantoms were selected in order to show the object dependence of f_E. The chest phantom has different projection data from each view and simulates human anatomy. The circular phantom has a smaller total volume than the chest phantom and the projection data are the same for each view. The sheet phantom permits studying the correction factor as a function of thickness.

The values of f_E are plotted as a function of view number for the circular and elliptical phantoms in Figure 1A. This graph illustrates the small variation of the emission correction factor as a function of object and imaging geometry. The relative difference between the minimum and maximum value for the elliptical phantom is 0.88%. The relative difference between the average value for the ellipse and the circle is 0.90%. There is a small relative difference between the values for the phantoms and the value with no phantom: 2.1% for the circular phantom and 3.0% for the elliptical phantom.

Even though the variation in the compensation factor between the different phantom shapes is small, Figure 1A
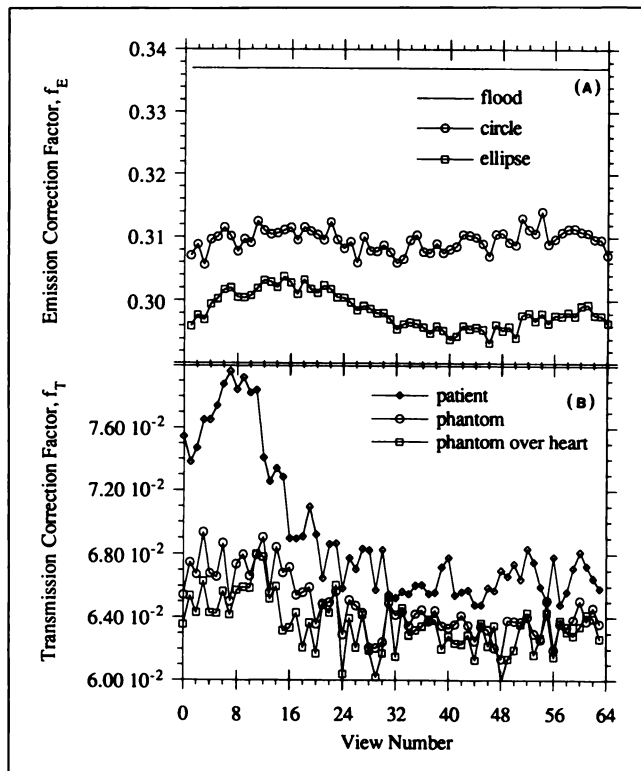
FIGURE 1. (A) Plot of the emission correction factor, f_E, versus view number. The factors are plotted for the cylindrical phantoms with circular and elliptical cross sections as well as for the flood source alone (no phantom). (B) Plot of the transmission correction factor, f_T, versus view number. The factors were computed using patient data, the full phantom data, and the phantom data from a strip containing the cardiac insert.

FIGURE 2. Plot of the emission correction factor, f_E, as a function of the water-equivalent thickness of the Lucite absorber between the camera and the transmission source. The solid line represents a fit with a second order polynomial.

suggests that the emission correction factor depends on the size and thickness of the phantom. To study this dependence, we measured the emission correction factor as a function of object thickness using the sheet phantom. The results are shown in Figure 2. In this figure the object thickness has been converted to water equivalent thickness by multiplying by the ratio of the observed linear attenuation coefficient for the Lucite sheets, 0.162 cm^{-1}, divided by that for water at 140 keV, 0.153 cm^{-1}. As Figure 2 shows, the value of the emission correction factor is large for small object thicknesses, decreases, reaches a minimum, and then increases.

This behavior can be understood in terms of the physical mechanisms causing the contamination. For thin objects, the number of multiply scattered photons is small and the contamination is dominated by Pb x-rays. As the thickness of the absorber is increased, the number of Pb x-ray photons produced by interaction with the transmission source collimator relative to the number of primary 140 keV photons decreases as a result of the higher attenuation coefficient in the object for the lower energy x-rays. This results in a decrease in the relative contamination and thus a decrease in f_E. However, as the thickness of the absorber increases further, the number of multiply scattered pho-
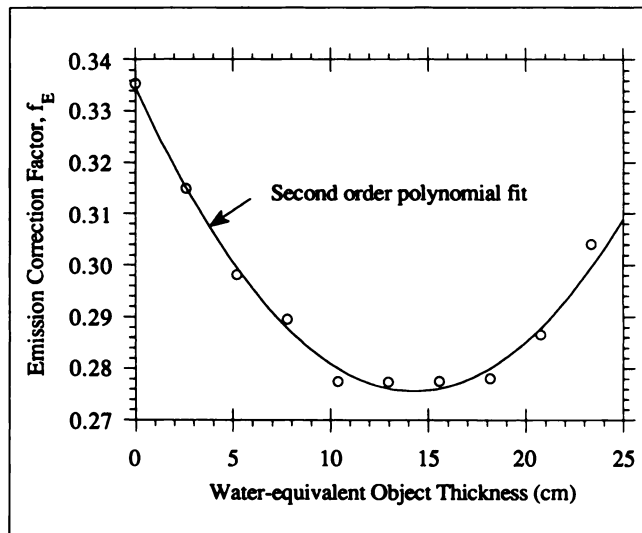
tons increases relative to the number of primary photons, resulting in an increase in f_E.

The solid curve in Figure 2 represents a second order polynomial fit to the data. Over the thickness range from 0 to 25 cm, this provides a very good estimate of the value of f_E given by:

$$f_E = 0.335 - 8.27 \times 10^{-3} \cdot t + 2.90 \times 10^{-4} \cdot t^2, \quad \text{Eq. 5}$$

where t is the water-equivalent thickness in centimeters.

The calibration curve was found to vary by several percent over the course of several months. However, the factors determined by using Equation 5 can be used by multiplying them by the ratio of the value of f_E determined each day using a flood source with no absorber divided by the value obtained using Equation 5 at zero depth.

The dependence of f_E on object thickness for the sheet phantom can be used to estimate the value of f_E for a complex phantom. Let T_i^0 and T_i be the transmission data from the ith pixel with and without the object, respectively, and μ be the attenuation coefficient of water for 140 keV photons. Then the water-equivalent thickness of the object in the ith pixel, t_i, is given by:

$$t_i = \frac{1}{\mu} \ln \frac{T_i^0}{T_i}. \quad \text{Eq. 6}$$

To apply Equation 6, we must have an estimate of the true transmission data for the pixel, T_i. Provided we know f_T and f_E, we can estimate T_i using Equation 4. However, f_E enters this equation only through the term $1/(1-f_E f_T)$. As we will see below, the transmission correction factor is small, on the order of 0.07. Thus, an error in estimated f_E will have only a small effect. As a result, for the purpose of estimating T_i for use in Equation 6, we can estimate f_E

using Equation 5 and an estimate of the average thickness of the patient.

Since the values of T_i used in Equation 6 were estimated using noisy data, the emission correction factors obtained with Equation 5 will also be noisy. To reduce this noise, the correction factors should be low pass filtered. To avoid introducing negative values, a frequency domain Gaussian-shaped filter was used. In this work, the filter had an equivalent spatial full width at half maximum of one pixel.

The effectiveness of Equations 5 and 6 in estimating the contamination in the emission image was verified using the chest phantom. In Figure 3, the contamination estimated from these equations using the measured transmission and emission data is compared to the measured contamination. The figure shows a horizontal profile through the measured and estimated contamination images for the left lateral projection. The estimated contamination is within the error bars of the measured projection data for most points, especially in the area of the profile coincident with the phantom. Similar agreement was observed for other projection views.

Transmission Correction Factor

The transmission correction factor, f_T, was determined by acquiring data in both the emission and transmission windows using only an emission source for both the chest phantom and a patient. The object dependence of the transmission correction factor was assessed by comparing the value computed in two regions in the chest phantom: (1) the entire image (global) and (2) a strip 10 pixels wide containing the heart (local). The resulting transmission correction factors are plotted as a function of view number in Figure 1B.

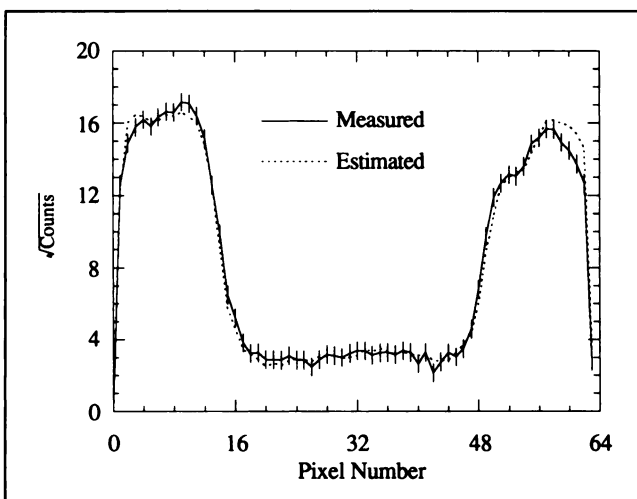Global values of f_T were determined for the patient and

phantom using data from all views. The relative difference between these values was 5.8% with respect to the mean. From Figure 4, we see that there is also a large variation in the transmission correction factor for the same object viewed from different angles. The differences relative to the mean between the minimum and maximum values were 12% and 20% for the phantom and patient, respectively. As can be seen from Figure 1B, there is relatively little difference in the value of f_T for the entire phantom and the region over the heart. The relative difference between the average value of the factor determined globally and over the heart was 1.8% with respect to the mean.

These results demonstrate that the transmission correction factor is much more object and geometry dependent than the emission correction factor. To avoid measuring this factor for each patient and view, thereby performing the equivalent of a separate acquisition, we will use a single average correction factor to compensate all the data. A reasonable estimate of this average factor can be obtained by averaging the factors determined from the left lateral and anterior views (view numbers 16 and 48, respectively). For example, the values for the transmission correction factor determined by averaging the correction factors from these two views for the patient, entire phantom, and
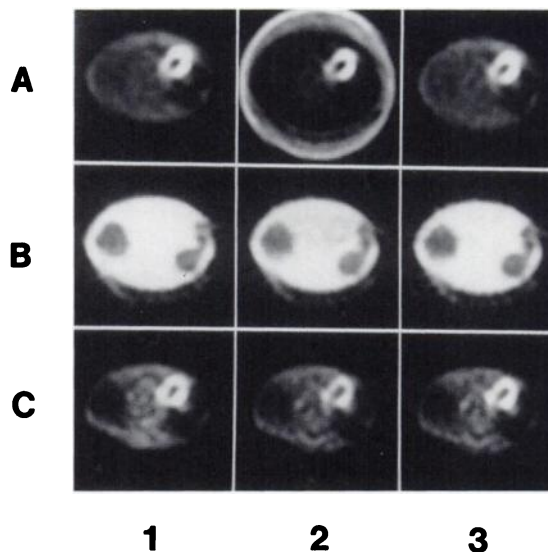

FIGURE 4. Transaxial images reconstructed from various chest phantom projection data sets. (Row A) Emission images reconstructed without attenuation compensation using FB. (Row B) Transmission images reconstructed using FB algorithm. (Row C) Emission images reconstructed using ML-EM and the attenuation maps from the corresponding images of row B to perform nonuniform attenuation compensation. (Column 2) Emission images reconstructed without attenuation compensation using FB. Images reconstructed from simultaneously acquired data without cross-contamination compensation (except Row C, where the image was reconstructed using cross-contamination compensated emission data and the attenuation map reconstructed from uncompensated data.) (Column 3) Images reconstructed from simultaneously acquired data following cross-contamination compensation.

FIGURE 3. Plot comparing the measured and estimated contamination in the emission energy window. The estimate was calculated using Equations 5 and 6. The plot is of the projection data from the left lateral view of the chest phantom (view number 16) from a slice passing approximately though the center of the phantom.

phantom in the cardiac area differ by 0.7%, 0.8% and 1.8%, respectively, relative to the average value from all views. We will investigate below the use of this single estimated correction factor to compensate for the cross-contamination of simultaneously acquired emission and transmission images.

Cross-Contamination Compensation

In the previous two sections, data were presented to show that estimating the transmission and emission correction factors for each patient is possible with reasonable accuracy. A single average value of the transmission correction factor can be estimated from a lateral and anterior image acquired without the transmission source. The emission correction factor can be determined from the water-equivalent thickness of the object in each pixel. These thicknesses can be determined from the simultaneous transmission data and the flood image. These results suggest the following protocol for compensating for cross-contamination in the simultaneously acquired data:

1. Estimate of the transmission correction factor, f_T, as the average of the factors from left lateral and anterior views acquired without the transmission source.
2. Generate an initial estimate of the transmission data using Equation 4, the value of f_T from Step 1, and a preliminary estimate of f_E based on Equation 5 and a depth of 10 cm.
3. Compute the final emission correction factor, f_E, for each pixel using the initial estimate of the transmission data calculated in Step 2 and Equations 5 and 6.
4. Scale the emission correction factor images obtained in Step 3 by the ratio of f_E observed for the flood phantom for the current patient divided by the value from Equation 5 evaluated at zero thickness.
5. Filter the correction factor images from Step 4 using a Gaussian filter.
6. Generate the cross-contamination compensated emission and transmission data using Equations 3 and 4, the value of f_T obtained in Step 1, and transmission correction factor images (f_E) obtained in Step 5.

Evaluation of Compensation Technique: Phantom Study

We have evaluated the effectiveness of the above compensation technique using chest phantom transmission and emission data sets that were acquired simultaneously and separately. The simultaneously acquired data was processed as described above. The resulting cross-contamination compensated projection data were constructed using the FB algorithm. The resulting images demonstrate the effectiveness of the compensation scheme for the emission and transmission data individually. To show the combined effect of the contamination compensation procedure, the emission data were also reconstructed using 50

iterations of the ML-EM algorithm including nonuniform attenuation compensation using an attenuation map reconstructed from the transmission data.

The resulting images, shown in Figure 4, demonstrate the effectiveness of the compensation technique in reducing cross-contamination of the emission and transmission data. From this figure, we see that the emission, transmission, and attenuation compensated emission images (Rows A, B and C, respectively) reconstructed from the simultaneously acquired data without cross-contamination compensation (Column 2) have significant artifacts and inaccuracies as compared to those reconstructed from the separately acquired data (Column 1). However, the images reconstructed from simultaneously acquired data with cross-contamination compensation (Column 3) appear qualitatively similar to the those reconstructed from separately acquired data.

To amplify the differences, Figure 5 shows images resulting from subtracting the simultaneously acquired data without (Row A) and with (Row B) cross-contamination compensation from images reconstructed from separately acquired data. The intensity to gray-scale mapping was different for each image in Figure 5, so comparisons of the absolute size of the errors in different images are not possible. In the images reconstructed from data without cross-contamination compensation, we observe: a large ring artifact in the emission image (Fig. 5 A1); reduced values of the attenuation coefficient in the transmission image (Fig. 5 A2); and significantly reduced intensity in the region of the myocardium in the attenuation compen-
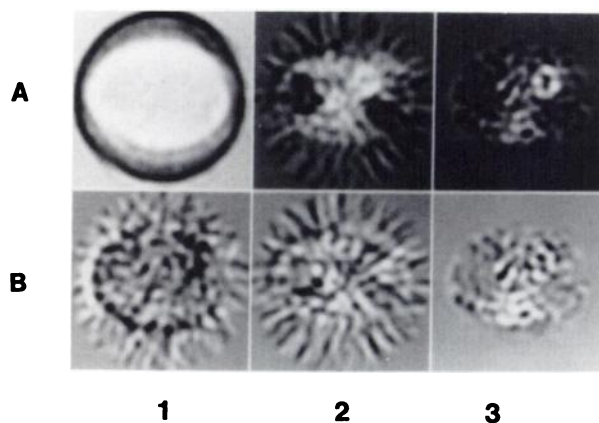

FIGURE 5. Difference images resulting from subtracting the transaxial images shown in Figure 4. (Row A) Separately acquired minus simultaneously acquired, uncompensated images. (Row B) Separately acquired minus simultaneously acquired, compensated images. (Column 1) Emission images reconstructed without attenuation compensation using FB. (Column 2) Transmission images reconstructed using FB. (Column 3) Emission images reconstructed using ML-EM with nonuniform attenuation compensation. (For the image in Column 3, Row A, the cross-contamination compensated emission data were reconstructed using the attenuation map reconstructed from the uncompensated transmission data.) Each image is displayed with the minimum pixel value in the image mapped to black and the maximum mapped to white.
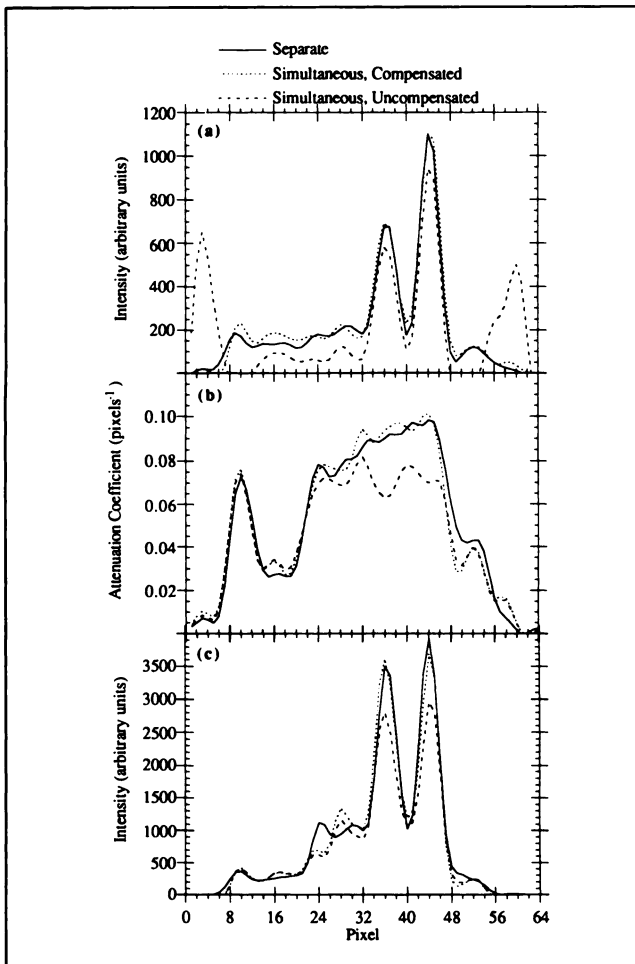
FIGURE 6. Plots showing horizontal profiles through the center of the heart from the images in Figure 4. The plots compare images reconstructed from separately acquired data (solid line) and simultaneously acquired data with (small dash) and without (large dash) cross-contamination compensation. The images used for each profile come from the corresponding rows of Figure 4.

sated emission image (Fig. 5 A3). For the images reconstructed from the simultaneously acquired cross-contamination compensated data, there is little systematic error, as illustrated by the images in Figure 5, Row B.

The profiles in Figure 6 show that there is good quantitative agreement, for both emission (Fig. 6b) and transmission (Fig. 6b) images, between images reconstructed from separately acquired data and cross-contamination compensated simultaneously acquired data. The profiles in Figure 6c demonstrate that attenuation compensated emission images reconstructed from the cross-contamination compensated simultaneously acquired emission and transmission data are in good quantitative agreement with images reconstructed from separately acquired data. These results demonstrate the effectiveness of the cross-contamination compensation procedure.

The simultaneously acquired transmission data were also cross-contamination compensated using a different

transmission correction factor for each view and a transmission correction factor determined in the strip containing the heart. No significant difference was observed when using these factors compared to using the single global transmission correction factor. As a result, we conclude that the use of a single global transmission correction factor is an acceptable approximation.

Evaluation of Compensation Technique: Patient Study

The compensation technique was also applied to patient data. The compensated emission and transmission projection data were calculated from the measured data using the procedure described above. The resulting projection data were reconstructed using the ML-EM algorithm with truncation compensation and with and without attenuation compensation. As a result of patient motion between the studies, a direct quantitative comparison of the emission images is not possible. No separate transmission-only study was performed, due to time and patient discomfort limits.

Figure 7 shows that the emission image reconstructed from the compensated data (Fig. 7b) is noisier but otherwise of comparable quality to the separately acquired emission image (Fig. 7a). The transmission image reconstructed from the compensated data (Fig. 7d) looks good qualitatively. The emission image reconstructed using the attenuation map and the simultaneously acquired emis-
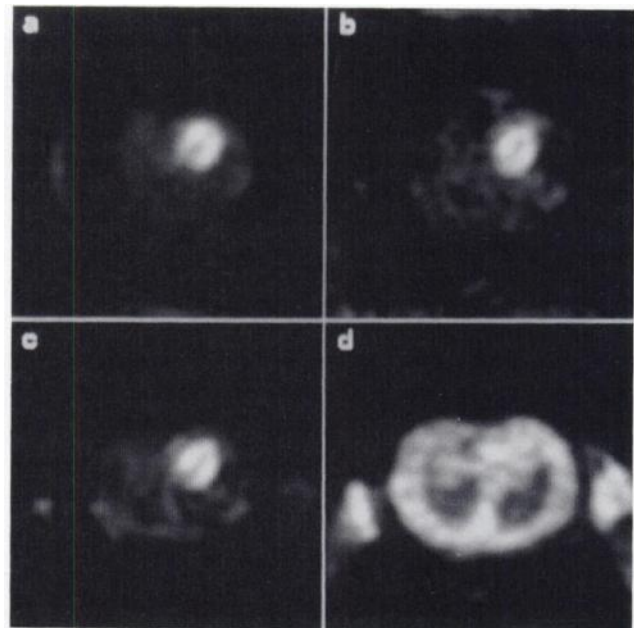

FIGURE 7. Transaxial images of a patient reconstructed using ML-EM including truncation compensation from separately and simultaneously acquired projection data. The images shown are: (a) emission image reconstructed from separately acquired data; (b) emission and (c) transmission image reconstructed from simultaneously acquired data with cross-contamination compensation; and (d) emission image reconstructed with nonuniform attenuation compensation from simultaneously acquired cross-contamination compensated data using the attenuation map in (c).

sion data is shown in Figure 7c. Again, the image quality is good and is better than that of the image reconstructed without attenuation compensation (Fig. 7b).

CONCLUSIONS

Attenuation maps measured using transmission computed tomography techniques are useful for nonuniform attenuation compensation in SPECT imaging. To avoid the additional time required for another acquisition and difficulties involved in registering the data, it is desirable to acquire the emission and transmission data simultaneously. In this work, we have described a technique requiring minor equipment modifications and using readily available isotopes for simultaneously measuring emission and transmission data in ^{201}Tl SPECT. This technique is based on the use of a ^{99m}Tc transmission source combined with postacquisition image processing to compensate for the cross-contamination between the transmission and emission projection data.

The compensation technique requires the determination of two correction factors. The transmission correction factor, which is more object-dependent, can be determined from two additional static emission images of the patient acquired at left lateral and anterior positions. It is calculated by performing a weighted fit of a line through the origin to a plot of the counts in the transmission versus emission energy windows. The emission correction factor can be determined using the simultaneously acquired data and a calibration curve that gives the value of the factors as a function of absorber thickness. This calibration should be performed once for each imaging system.

When the technique was applied to a chest phantom, there was excellent quantitative agreement between transaxial images reconstructed from the compensated and separately acquired data. Though no direct quantitative comparison could be made in the patient study performed, there was qualitative agreement between the images reconstructed from simultaneous and separate acquisition data.

This technique provides a simple and effective method for determining attenuation maps. These attenuation maps, combined with algorithms that compensate for nonuniform attenuation, result in improved quantitative information from ^{201}Tl cardiac SPECT.

ACKNOWLEDGMENTS

REFERENCES

1. Gullberg GT, Huesman RH, Malko JA, Pelc NJ, Budinger TF. An attenuated projector-backprojector for iterative SPECT reconstruction. *Phys Med Biol* 1985;30:799-816.
2. Malko JA, Heertum RLV, Gullberg GT, Kowalsky WP. SPECT liver imaging using an iterative attenuation correction algorithm and an external flood source. *J Nucl Med* 1986;27:701-705.
3. Tsui BMW, Gullberg GT, Edgerton ER, et al. Correction of nonuniform attenuation in cardiac SPECT imaging. *J Nucl Med* 1989;30:497-507.
4. Fleming JS. A technique for using CT images in attenuation correction and quantitation in SPECT. *Nucl Med Commun* 1988;10:83-97.
5. Bailey DL, Hutton BF, Walker PJ. Improved SPECT using simultaneous emission and transmission tomography. *J Nucl Med* 1987;28:844-851.
6. Tan P, Bailey DL, Hutton BF, et al. A moving line source for simultaneous transmission/emission SPECT. *J Nucl Med* 1989;30:964.
7. Perry JR, Tsui BMW. Optimization of collimator design and acquisition parameters for cardiac ^{201}Tl studies. *J Nucl Med* 1990;31:870.
8. Shepp LA, Vardi Y. Maximum likelihood estimation for emission tomography. *IEEE Trans Med Imaging* 1982;1:113-121.
9. Lange K, Carson R. EM reconstruction algorithms for emission and transmission tomography. *J Comput Assist Tomogr* 1984;8:306-316.